Research papers

Synergistic effect of two-dimensional additives on carbon nanotube film electrodes towards high-performance all-solid-state flexible supercapacitors

Sunil P. Lonkar [*], Zainab Karam, Abdulrahman Alshaya, Myriam Ghodhbane, Juveiriah M. Ashraf, Vincenzo Giannini, Chiara Busa [*]

Energy Storage Group, Advanced Materials Research Center, Technology Innovation Institute, Masdar City, Abu Dhabi, P.O Box 9639, United Arab Emirates

ABSTRACT

Flexible supercapacitors (SCs) have attracted growing interest as the power source for portable and wearable electronics. In the present work, we report the CNTs (Carbon Nanotubes) buckypaper integrated with electro-active 2D materials including graphene, graphene oxide (GO), and transition metal sulphides (TMDs), especially tin sulphide (SnS_2). The flexible and free-standing, interface-enhanced CNT paper having homogeneously dispersed 2D materials was prepared using a traditional scalable casting method. The hybridized CNT films were thoroughly characterized to elucidate their structural and surface properties. Finally, such hybrid CNT films were used as free-standing electrodes without any binder for the fabrication of flexible-solid-state supercapacitor (FSSSs) devices. In the FSSS, the electrochemical interactions between hybrid CNT paper electrodes and a polymer gel electrolyte were studied. In the symmetric configuration, the CNT-SnS_2 electrodes reach the highest areal and volumetric capacitance of 533 mF/cm^2 and 63 mF/cm^3, respectively, almost four times that of pristine CNT electrodes, whereas CNT-GO-based electrodes display high-rate capability. The CNT-SnS_2-based symmetric FSSS devices exhibit an extended voltage window of 1.5 V with a high capacitance of 133 mF/cm^2 and show high cyclic stability for 5000 cycles under 180^0 bendings.

1. Introduction

Flexible and miniaturized electronic devices have attracted widespread attention due to their potential for future hand-held, portable consumer, and wearable electronics [1,2]. This has incited a growing interest in the development of compact yet efficient power sources that are flexible and holds the potential to be implemented in confined space for newer applications. In this advent, the flexible supercapacitor is considered an attractive energy storage device, filling the gap between batteries and conventional supercapacitors [3,4]. Owing to their excellent stability, safety, and ability to also store or convert energy upon bending or repeatedly folding without lessening their performance, flexible supercapacitors surpass conventional energy storage devices [5,6]. Hence, flexible supercapacitors, with faster charging or discharging rate capability, longer life cycles, and higher energy density, are gaining significant interest in the electrical energy storage field. Furthermore, a free-standing, ultrathin, miniaturized, and binder-free electrode with large capacitance and low cost is an urgent requirement for flexible supercapacitors [7–9].

Recently, carbon nanotubes (CNTs) have emerged as promising materials for efficient, flexible supercapacitor electrodes owing to their excellent high electrical conductivity, high mechanical strength, large surface area, sizeable porous structure, and functionalization ability [10–12]. Moreover, the CNT-based nanostructures in their macroscopic forms, such as three-dimensional (3D) aerogels, two-dimensional (2D) porous sheets, and spherical zero-dimensional (0D) forms, find their applications in diverse fields [12,13]. The CNTs in the form of a two-dimensional sheet, called bucky paper, are the best-suited and most commonly used electrode materials in fabricating flexible supercapacitors [14,15]. However, due to its limited charge storage capabilities, the performance of the CNT film-based supercapacitors still does not match the average performance of commercial solutions. Thus, various electroactive additives were introduced using different methodologies to improve the charge storage performance of such CNT films for flexible supercapacitors.

Two-dimensional (2D) materials, including graphene and its derivatives, were commonly used as electrode materials in SCs because of their high electrical conductivity and surface properties [16,17]. On the

---

other side, 2D materials based on transition metal dichalcogenides.

(TMDs)/oxides (TMOs) have attracted tremendous attention owing to their similarities with graphene and redox-active properties that can lead to pseudocapacitive charge storage [18–25]. Hence, introducing these 2D materials into CNTs is expected to create a hybrid structure with tailored surface and electrical properties, which could favour rapid ionic diffusion through electrodes. Recently, Wang et al. [26] introduced MoS_2 nanoparticles on the CNT network and further coated with reduced graphene oxide (RGO), the resulting CNT hybrid was used as electrode material and PVA-H_2SO_4 gel as an electrolyte to assemble a flexible symmetric supercapacitor device to attain a high areal capacitance of 109 mF/cm^2. Similarly, Zhou et al. [27] prepared SnS_2 anchored functionalized carbon cloth for flexible supercapacitor application with a capacitance of 194.4 mF/cm^2. Similarly, Tiwari et al. [28] synthesized the CNT/MoS_2 hybrid nanostructures as electrodes for solid-state supercapacitors, and the electrode possesses a high areal capacitance of 337 mF/cm^2 Balboni et al. [29] reported the hybrid electrodes composed of CNT/polyaniline/PDMS to assemble a flexible supercapacitor and exhibit a capacitance of 408 mF/cm^2. Also, Wang et. Al. [30] used 2D WS_2 integrated CNT thin films as hybrid electrodes for flexible supercapacitors having their symmetric device achieved capacitance up to 575 mF/cm^2. Among these TMD-based 2D materials, layered tin disulfide (SnS_2) based electrode materials have attracted extensive interest as electrode materials in energy storage applications primarily because of their high theoretical capacity, layered structure with weak van der Waal interactions, natural abundance, good mechanical stability, low-cost and high faradic behaviour, etc. [31–33]. Overall, these studies highlight the significance of introducing electro-active additives, especially 2D materials, that can elevate the charge storing capability of CNTs especially in assembling a high-performance flexible supercapacitor. However, the preparation of most of these CNT-based 2D nanohybrid electrode materials is realized using highly tedious and intricate methods such as solvothermal, hydrothermal, vapor phase deposition techniques, etc., which significantly impeded their large-scale implementations. Hence, a preparation method that can uniformly integrate these 2D electroactive additives into the commercially produced CNTs and that is scalable, environmentally benign, and cost-effective is greatly sought.

Herein, we report a facile method of solution dispersion and casting to produce flexible and porous films using the 2D materials integrated into commercially produced CNTs. The resulting free-standing, binder-free, flexible, and lightweight hybrids were used as current collector-less electrodes to assemble a flexible all-solid-state symmetric supercapacitor device. The selected electroactive 2D materials were tin sulphide (SnS_2), graphene oxide (GO), and thermally reduced graphene oxide (TRG). The as-obtained porous CNT hybrid film electrodes were expected to show significant synergistic effects in elevating the electrochemical performance. The impact of 2D materials on the morphology and structural features as well as their synergistic effect on the electrochemical performance of the resulting CNT nanohybrid electrodes, were discussed in detail. The hybrid electrodes were further used to assemble flexible solid-state symmetric supercapacitors, with PVA/LiCl as the solid electrolyte and the separator. Similarly, the electrochemical performance of the resulting device after 180^0 bending and the performance of the 2-in-1 series connection is also discussed in detail.

2. Experimental sections

2.1. Materials

All chemical reagents in this experiment were of analytical grade and used as received. Multi-walled carbon nanotube (MWCNT) flakes (hereafter termed as CNTs) were obtained from Applied Nanostructured Solutions, LLC (USA), a spin-off company of the Lockheed Martin Corporation. Polyvinyl alcohol (PVA, Mw: 120000) was purchased from

Alpha Chimika, India, and LiCl was received from Sigma-Aldrich Chemical Company. Graphene oxide (GO) aqueous dispersion (4 mg/ml) was purchased from Advanced Graphene Products. Tin disulphide (SnS_2) 2D nanosheets and thermally reduced graphene oxide (TRG) were prepared as per our previous reports, respectively [34,35]. The structural morphology of the used 2D materials is presented in the Fig. S1.

2.2. Preparation of pristine CNT flexible film

The as-received CNTs pellets (200 mg) were first grounded in 10 ml of a mixed solvent of water: ethanol (1:1), then the resulting CNT mix was further diluted with 50 ml aqueous ethanolic solvent and subjected to the probe sonication for 10 min at 40 % amplitude. The resulting dispersion was continuously stirred during the sonication. A significant increase in the viscosity of the resulting dispersion was noted. Later, the as-obtained slurry was carefully cast on copper foil using the doctor blade method using a pre-set thickness of 5 mm for wet casting. The casted slurry was left for drying at ambient temperature. A smooth paper-like film was carefully peeled off the copper foil and used for further study. The thickness of the resulting films was measured to be between 50 and 70 μm.

2.3. Preparation of CNT hybrid flexible film with 2D materials

2.3.1. CNT-SnS_2 film

The CNT-SnS_2 hybrid film was obtained following a similar procedure used for pristine CNT film. The 40 mg of SnS_2 nanoplatelets were dispersed into 10 ml ethanol using the bath sonication for 10 min. In another flask, 160 mg of CNTs were dispersed in water: ethanol mixture (20:30 ml) under probe sonication. After 5 min, the SnS_2 dispersion was slowly added to the CNT dispersion under stirring and sonication and continued for another 5 min. The final weight ratio between CNT and SnS_2 was 80:20 % *w*/w. The casting and drying were carried out following the pristine CNT film procedure.

A similar procedure was employed to prepare the CNT hybrid films by introducing other 2D materials i.e., graphene oxide and TRG (CNT: 2D additive, 80:20 wt%) as per the procedure described for CNT/SnS_2 hybrid films. The thickness of all the CNT hybrid films ranged from 50 to 70 μm.

2.4. Preparation of PVA-LiCl polymer gel electrolytes

The PVA-LiCl-based neutral polymer gel electrolyte was prepared using a PVA: LiCl molar ratio of 1:1. First, the PVA gel was prepared by dissolving 1 g of PVA in DI water (10 ml) with continuous stirring at 80 °C until the formation of a clear gel. Separately, the aqueous LiCl solution was prepared by dissolving the 1 g LiCl powder in 10 ml DI water. Subsequently, the LiCl solution was added to the PVA gel and stirred at 80 °C until the homogeneous transparent gel electrolyte was obtained. After cooling down, the resulting polymer gel electrolyte was used for further studies.

2.5. Fabrication of flexible all-solid-state symmetric supercapacitors (FSSCs)

The flexible solid-state symmetric supercapacitor (SSC) device was assembled using either pristine CNT, CNT-SnS_2, CNT-GO, and CNT-TRG current collector-less electrodes as the positive and negative sides, respectively. Before fabrication, the stripped positive electrode was uniformly coated with the PVA-LiCl polymer gel electrolyte, and the same acted as a porous ion separator for the FSSC. One more CNT hybrid electrode strip was then stacked upon the electrolyte-applied electrode strip. Together, the assembly was uniformly pressed and wrapped with Kapton tape to obtain an FSSC device with high integrity. An expanded view an actual photograph of the flexible all-solid-state supercapacitor
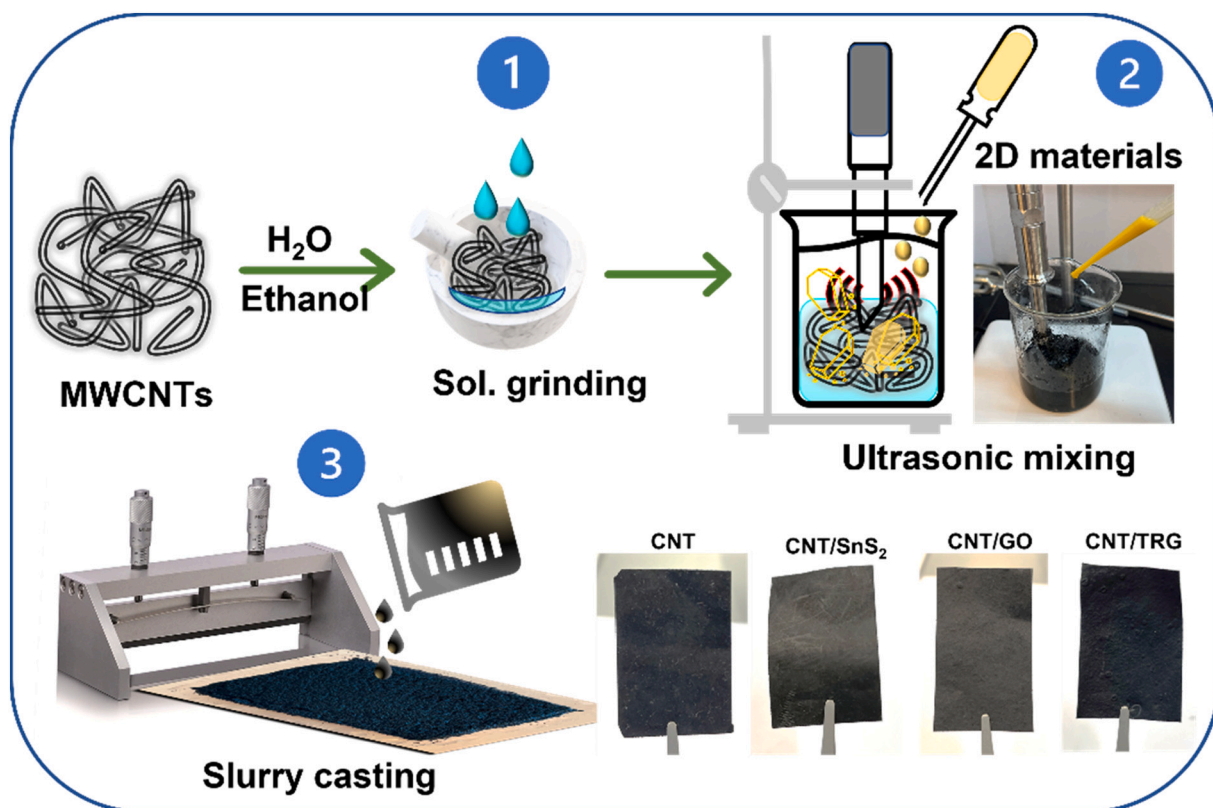
Fig. 1. Schematic illustration for the preparation of CNT-2D material hybrid electrode film and digital images of the resulting free-standing films of CNT, CNT-SnS$_2$, CNT-GO, and CNT-TRG, respectively.

made with the CNT hybrid electrodes as illustrated in Fig. 7a.

2.6. Material characterization

The structural features of the obtained 2D materials infused CNT hybrid films were characterized by various techniques. The morphology, porous structure, and element composition, along with their distribution within the CNT matrix, were investigated of dual-beam Scios2 microscope (Thermo Fisher Scientific) coupled with Oxford Ultimax 40mm^2 EDS elemental mapping tool. The effect of 2D additives on structural features of CNTs was further characterized by Raman spectroscopy. Raman spectra measurements with a 532 nm laser were used with an iHR550 spectrometer (Horiba LabRaman Soleil), and the signal of silicon was used as a reference. X-ray diffraction (XRD) analysis was used to understand the crystalline features of the resulting CNT hybrid films. The XRD was collected by a Bruker D8 Advance X-ray diffractometer within the scanning range from 2θ = 10° to 60° with Cu Kα radiation (λ = 1.5406 Å) and a LYNXEYE XE-T detector. The N$_2$ physisorption tests were performed to measure the specific surface area of the prepared hybrid films. Around 60 mg of each sample were dried at 80 °C for 8 h and then analysed, with a Nova touch (LX^4) surface area and pore analyser in a relative pressure range between 0.1 and 0.3.

2.7. Electrochemical measurements

Similarly, the electrochemical performance of the as-prepared CNT hybrids electrodes and assembled FSSS device was investigated by cyclic voltammetry (CV), galvanostatic charge-discharge (GCD), and electrochemical impedance spectroscopy (EIS) using a VSP300 potentiostat (Bio-Logic Science Instrument, Seyssinet-Pariset, France) electrochemical workstation in the two-electrode system. The as-obtained hybrid films were directly used as sans binder and current collector. EIS test was performed in a frequency range between 0.01 Hz to 100 kHz

at an open-circuit AC amplitude of 10 mV.

The electrochemical parameters, such as specific capacitances, energy density, and power density, were estimated at ambient temperature. The specific areal capacitance C$_A$ (mF cm^{-2}) and the specific volume capacitance C$_V$ (mF cm^{-3}) for the assembled symmetric supercapacitor cell were calculated using the charge integrated from corresponding GCD curves according to the following formula:

$$C_{A_{cell}} = \frac{I\Delta t}{S\Delta V} \tag{1}$$

$$C_{V_{cell}} = \frac{I\Delta t}{v\Delta V} \tag{2}$$

where 'I' represents current intensity (A), ΔV was the potential range (excluding IR drop) in the discharge process, 'S' was the area of two electrodes (cm^2), and v is the volume of the device, including the two electrodes, and electrolyte and 'Δt' denotes discharge time (s) of the experimental charge-discharge curve [36].

Similarly, the specific capacitance with respect to the single electrode was calculated from the following formulae:

$$C_{A_{elec}} = \frac{2I\Delta t}{S\Delta V} \tag{3}$$

The energy density E (μW h cm^{-2}) and power density P (μW cm^{-2}) of the assembled device was measured by equations as follows:

$$E = \frac{1}{2}\left[\frac{C_A\Delta V^2}{3600}\right] \tag{4}$$

$$P = \frac{3600 \times E}{\Delta t} \tag{5}$$

In which C$_A$ are the areal and volumetric specific capacitances of the symmetric supercapacitor devices.
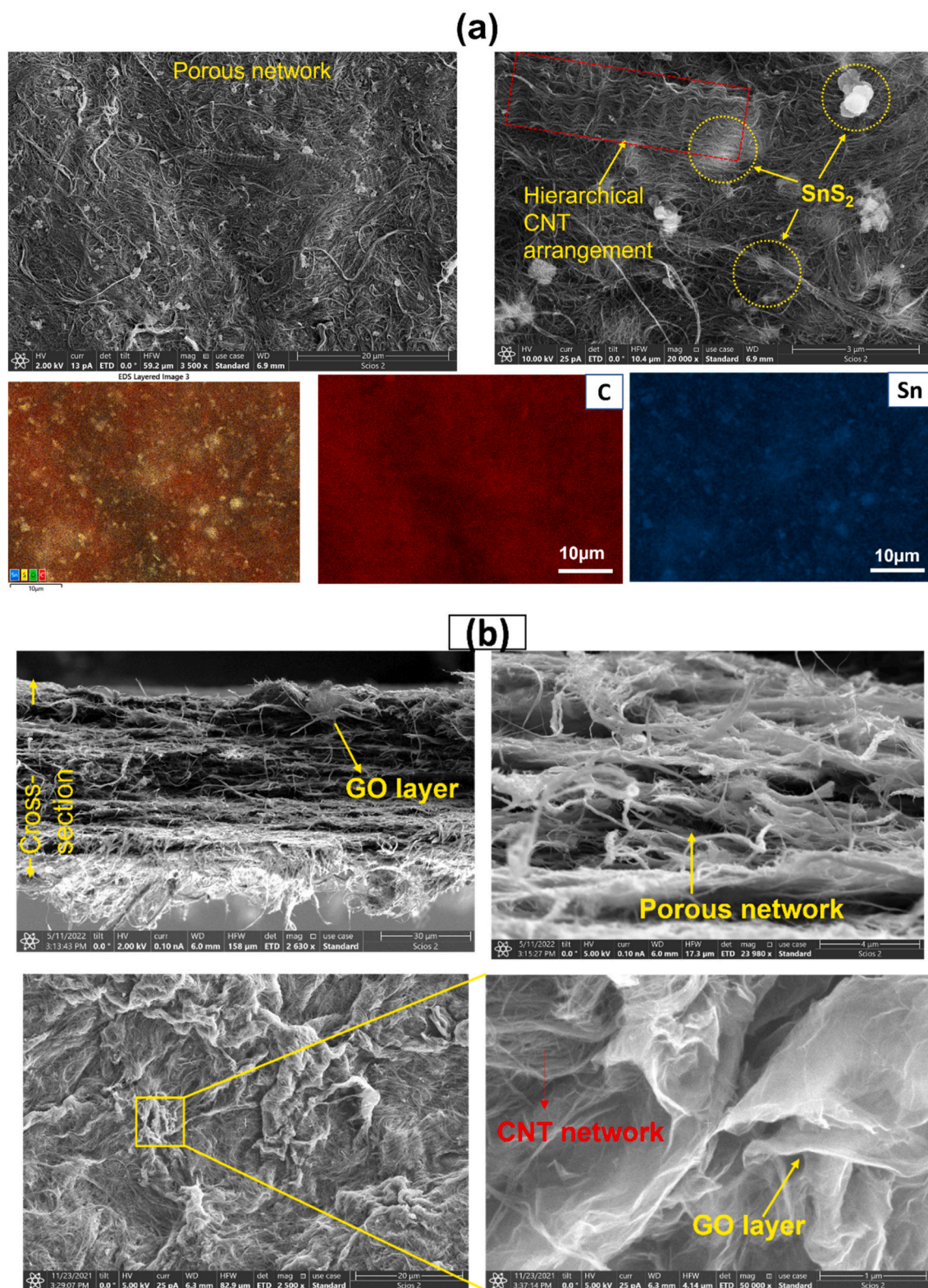
Fig. 2. Scanning electron images and EDS mapping showing the morphology and elemental composition of (a) CNT/SnS$_2$, and (b) CNT/GO hybrid films.

3. Result and discussion

Fig. 1 illustrates the schematic representation of the synthesis process for preparing 2D materials integrated with flexible CNT hybrid films. The 2D materials were uniformly dispersed and mixed with CNTs, the resulting slurry was then cast and dried to obtain a flexible that was used as an electrode to fabricate the symmetric all-solid-state supercapacitors.

By the microstructure and elemental composition analysis (Fig. 2), the pristine CNT sheet is comprised of a highly intermeshed tortuous network of carbon nanotubes (Fig.S1a). The hexagonal 2D SnS$_2$ sheets integrated CNT films show a well-spaced porous network with spatial
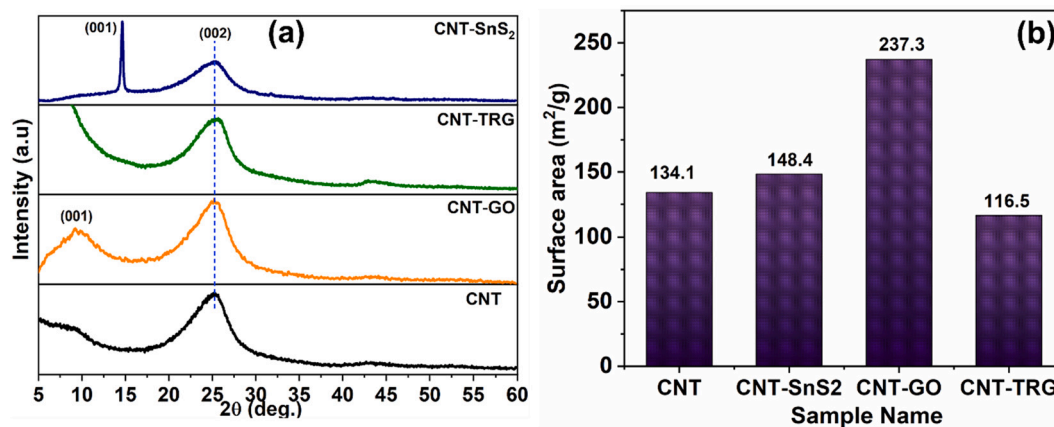
Fig. 3. XRD patterns (a) and BET surface areas (b) of CNT, CNT-SnS$_2$, CNT-GO, and CNT-TRG nanohybrid films.

and uniform distribution of SnS$_2$ nanoparticles within the CNT network (Fig. 2a). The internal organization in a layered fashion is observed, introducing an additional hierarchical level for carrier mobility. Within this multi-tiered organization, elements such as carbon, and tin are homogenously dispersed within the CNT network (Fig. 2a), further supporting our experimental approach. Moreover, the interfacial homogeneity between uniformly distributed SnS$_2$ and CNTs results into an inter-connected porous network of the hybrid film (Fig. S2). As shown in Fig. 2b, the GO-loaded CNT films form porous and densely dispersed GO layers with micron-sized folds resulting from the GO chemical interaction with the CNT surface [37]. However, the stacked GO sheets, which are electronically connected by the CNT network, show uneven localised features. In turn, the stretched irregular microporous network enables alternative pathways acting as diffusion channels to facilitate the ion's penetration in the bulk of the flexible electrode. Other samples, such as the thermally reduced graphene in CNTs (CNT-TRG), showed layers of graphene sheets were interconnected with the CNT network with a poorly dispersed state (Fig. S3). The higher degree of agglomeration of TRG in CNTs could be due to the repulsive forces between highly polar dispersion solvents and the relatively non-polar/hydrophobic character of TRG sheets.

The X-ray diffraction (XRD) was employed for structural and phase analysis of the resulting CNT-based nanohybrid films, and the resulting pattern was displayed in Fig. 3a. The diffraction pattern of the pristine CNT film shows a peak at $2\theta = 25.5°$, which is ascribed to the characteristic (002) plane from the graphite structure in the MWCNTs [38]. For the CNT-SnS$_2$ sample, the XRD pattern shows a sharp, intense peak at $2\theta = 14.6°$ arising from (001) plane reflection of hexagonal SnS$_2$ sheets [34] (Fig. S4) and a peak around $2\theta = 25.5°$ was attributed to the graphic (002) peak of CNTs. For CNT-SnS$_2$, a CNT peak broadening was observed, which can be attributed to the coarse CNT network due to the addition of 2D SnS$_2$ nanosheets. Similarly, GO-infused CNT sheets showed a peak around $2\theta = 9.3°$ indexed as (001) facet of GO and CNT peak around $2\theta = 25.3°$. The GO peak was observed to be shifted towards a lower angle compared to the pristine GO (Fig. S4) suggesting the exfoliated state of GO sheets in the resulting CNT-GO nanohybrid. Lastly, the CNT-TRG nanohybrid showed a coinciding XRD peak at $2\theta = 25.4°$ coming from the (002) plane of graphitic carbon in graphene and MWCNTs.

Fig. 3b illustrates a surface area comparison of different CNT nanohybrid films calculated from the N$_2$ isotherms. The surface area of the pristine CNT buckypaper film was measured to be 134.1 m^2/g, which is in line with the previous report [39]. The addition of SnS$_2$ leads to a slight increase in the surface area (148.4 m^2/g) of the CNT hybrid film, confirming the addition of 2D SnS2 sheets creates an improved porous network. Whereas the GO addition significantly increases the surface area to 237.3 m^2/g, which could be due to the interaction of GO layers
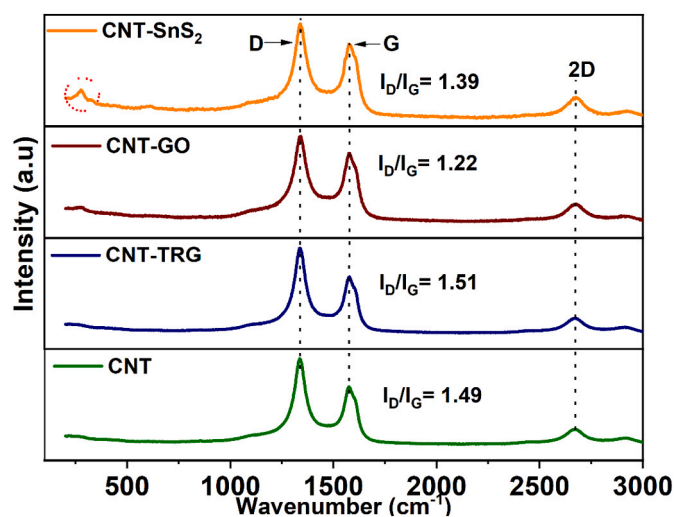
Fig. 4. Raman spectra of pristine CNT, CNT-SnS$_2$, CNT-GO, and CNT-TRG nanohybrid films.

with the CNTs creating a porous network structure as observed in the SEM (Fig. 2b). In the case of CNT-TRG, the surface areas were marginally decreased to 116.5 m^2/g due to the poor dispersion, which led to disruption in CNT porous structure (Fig. S3).

The structural features of resulting CNT nanohybrids were further investigated to the fine scale via Raman spectroscopy (Fig. 4). All samples showed the characteristic D and G bands attributed to the graphitic structure, which corresponds to the sp^3 and sp^2 hybridized state of carbon, respectively. These peaks are often considered metrics to evaluate the degree of disruption of π- π bonding in graphitic structures [40]. The addition of 2D materials leads to a change in I$_D$/I$_G$ ratio on account of their individual contribution to the Raman signals. The pristine CNT sheet shows characteristic Raman peaks i.e. D band around 1340 cm^{-1} corresponding to scattering originating from defects and disorders and G band around 1577 cm^{-1} which represent in-plane stretching of the C—C bonds in the graphitic carbon structure. The pristine CNT sheet gives I$_D$/I$_G$ ratio of around 1.49 and after the addition of TRG (I$_D$/I$_G$ = 1.51), no meaningful change was observed. The addition of GO i.e. CNT-GO leads to decreased I$_D$/I$_G$ = 1.22, indicating lowered concertation of sp^2 domains because of functional groups from GO [41]. For CNT-SnS$_2$, in addition to the D and G bands of CNT, a distinct peak around 310 cm^{-1} was representing the A$_{1g}$ mode of 2H-SnS$_2$ [42]. Overall, Raman results indicate that the original CNT structure is not significantly altered with the addition of 2D nanomaterials, inferring CNTs as the scaffold for
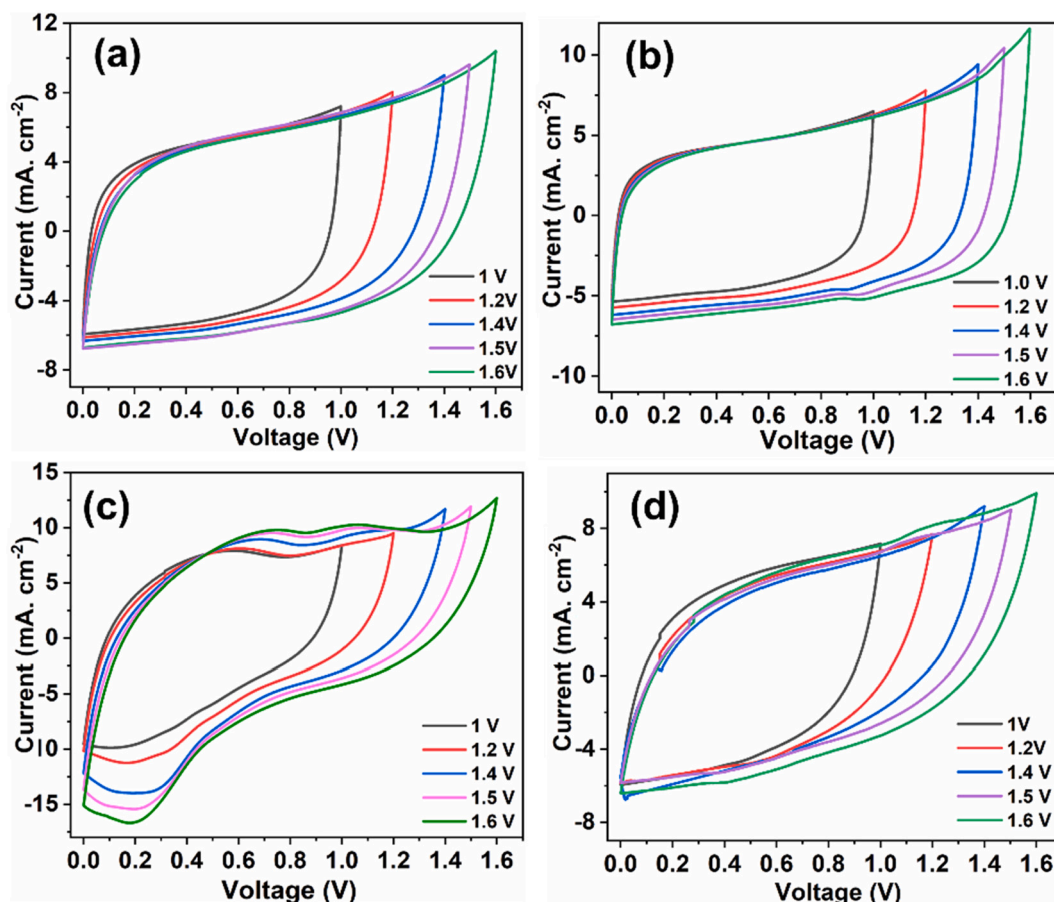
Fig. 5. Cyclic voltammetric curves with different working voltage windows measured at 50 mV/s scan rate for pristine a) CNT, b) CNT-SnS$_2$, c) CNT-GO, and d) CNT-TRG based symmetric flexible supercapacitor devices.
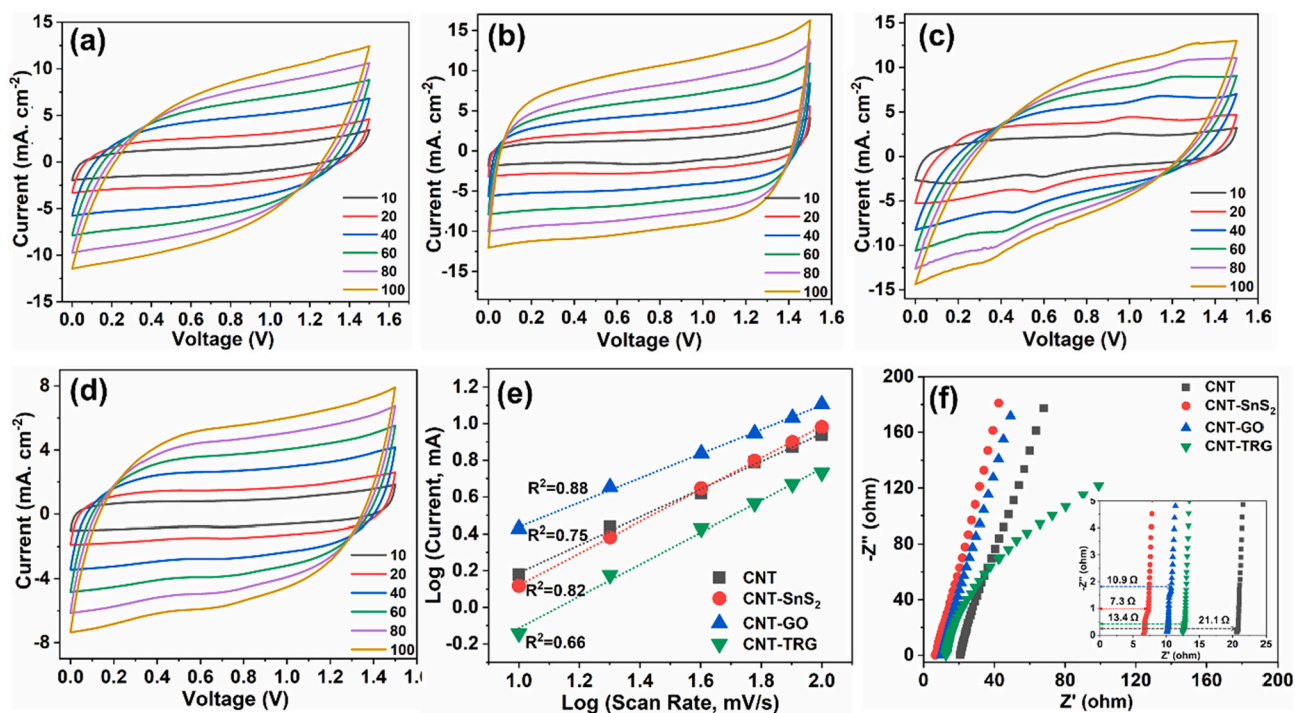
Fig. 6. Electrochemical characterization of pristine CNT, CNT-SnS$_2$, CNT-GO, and CNT-TRG based flexible solid-state symmetric supercapacitor devices: CV curves in the voltage window of 0–1.5 V at different scan rates (a-d), and the corresponding linear fittings of the log (peak current) versus log (scan rate) for the anodic peaks over (e), Nyquist plots over the frequency range of 0.1 Hz-100 kHz (the inset shows the close-up view of the high-frequency) (f).
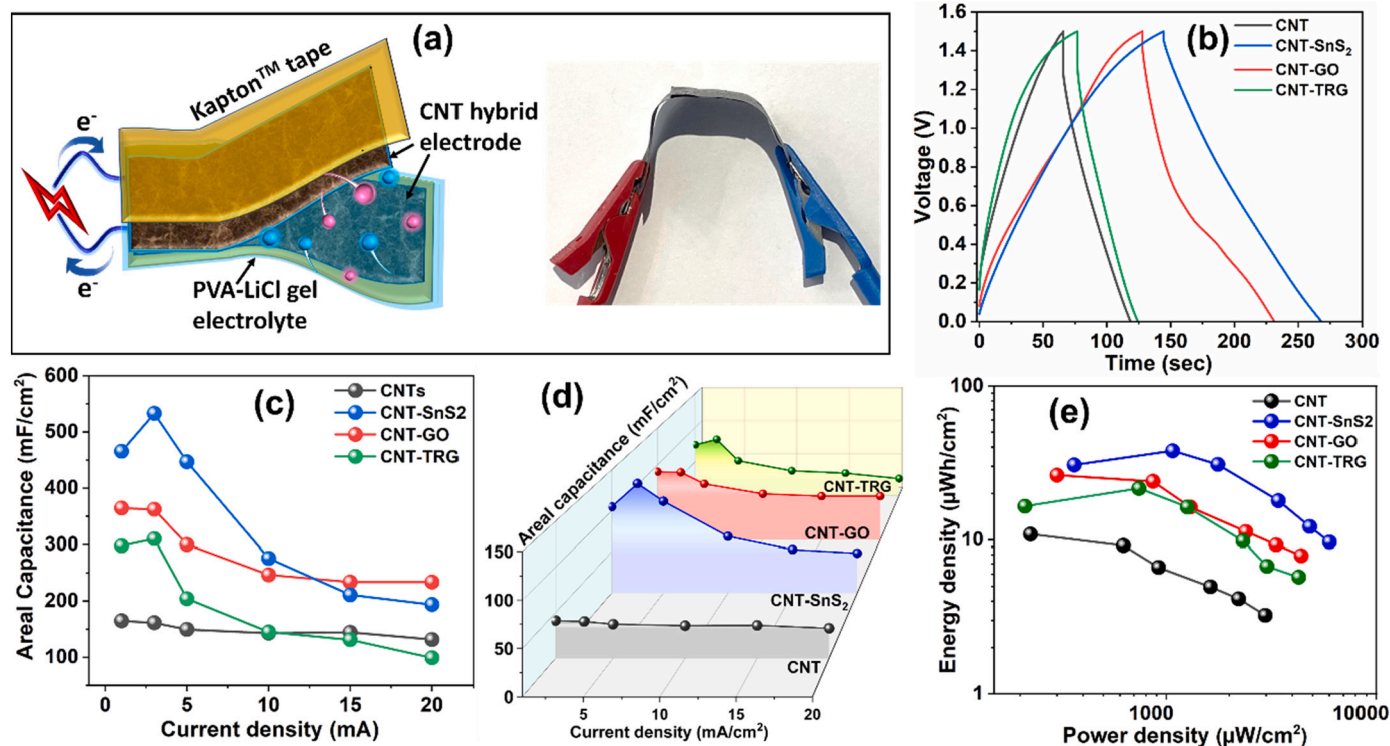
Fig. 7. Electrochemical properties of all-solid-state symmetric supercapacitors assembled using pristine CNT, CNT-SnS₂, CNT-GO, and CNT-TRG: (a) A schematic illustration of the solid-state device with PVA-LiCl polymer gel as the electrolyte and separator and a digital photograph of the assembled flexible symmetric supercapacitor device, (b) Galvanostatic charge/discharge curve measured at the current density of 3 mA, (c) Evolution of areal capacitance of single electrode versus current density, d) Evolution of areal capacitance of symmetric device versus current density, and e) Ragone plot derived from the resulting energy and power densities from all the CNT based hybrid devices.

physically hosting SnS₂ particles.

To evaluate the performance of as-obtained CNT hybrid film electrodes for practical supercapacitor applications, the all-solid-state symmetrical supercapacitor devices were assembled using LiCl-based polymer-gel electrolyte. The determination of practical capacitive voltage range and nature of charge storage mechanism is of foremost importance for the development of high-performance supercapacitor devices [43]. Hence, the symmetrical flexible SCs were assembled, and cyclic voltammetry (CV) was performed to estimate the maximum operating voltage in the range from 0.8 to 1.6 V at a scan rate of 50 mV/s as a function of the anodic vertex voltage (Fig. 5). Overall, the CV plots for pristine CNT-based device mostly display a quasi-rectangular shape with slightly symmetric humps at both ends with mostly EDLC-type charge storage behaviour (Fig. 5a). For CNT-SnS₂ (Fig. 5b), the CV curves also showed a symmetric rectangular shape with a weak redox peak indicating the combination of EDLC and redox charge storage mechanism and leap developing around 1.6 V. In the case of CNT-GO nanohybrids (Fig. 5c), the CV curves distinctly showed strong redox peaks demonstrating the strong pseudocapacitive behaviour and exhibit good voltage stability even at 1.6 V. The CV curves (Fig. 5d) for the CNT-TRG hybrid device displayed a typical quasi-rectangular shape assigned for EDLC charge storage. Overall, it is worth mentioning that the presence of a 'tail' at the vertex voltage is commonly adopted as evidence of any electrochemical reactions that occur in aqueous media. In the present study, all the CNT nanohybrid-based devices, which are scanned till 1.6 V as the maximum voltage started developing a tail after 1.5 V. Therefore, 1.5 V is considered a stable and wide voltage window for testing the CNT-based hybrid electrodes using a neutral LiCl polymer-gel electrolyte system.

To further investigate the electrochemical behaviour and the charge storage mechanism of the CNT hybrid paper, the assembled symmetric supercapacitor devices were subjected to CV scanning at different scan rates from 10 to 100 mV/s and impedance spectroscopy as shown in Fig. 6. Fig. 6a illustrates thugre CV plot of the pristine CNT paper-based device displays a mirror image-like behaviour electrochemical performance of the CNT-based flexible symmetric supercapacitor. For scan rates higher than 100 mV/s the shape of the CV curve remains semi-rectangular with no significant modifications to the ions insertion process into the electrode porous structure. Accordingly, the rapid formation of an electrochemical double layer translates to good electrochemical reversibility of the device. For the CNT-SnS₂ nanohybrid-based device (Fig. 6b), the CV retains its rectangular shape however, for scan rates lower than 40 mV/s, redox peaks were observed which highlights the pseudocapacitive behaviour of SnS₂ [44]. As the scan rate increases, the redox behaviour slowly gets diminished and typical rectangular CV behaviour was developed suggesting that at a high scan rate EDLC charge storage mechanism of CNTs is dominant over pseudocapacitive charge storage behaviour from SnS₂.

In the case of the CNT-GO hybrid (Fig. 6c), the CV curves show a typical rectangular shape with the addition of pseudocapacitive behaviour for various scan rates. In this instance, pseudocapacitance is likely a combination of charge storage mechanisms arising from both the electric double layer formation and the GO-bound functional groups actively participating in the redox reactions and occurring at the electrode interface [45], such as Eq. (6):

$$- C–OH \leftrightarrow C = O + H^+ + e^- \tag{6}$$

For the CNT-TRG hybrid electrode (Fig. 6d), the CV curves do not show any obvious redox peaks during the different scanning processes, which demonstrates the expected EDLC-type charge storage behaviour [46].

Another important parameter that governs the charge storage mechanism is the linear dependence of the anodic current with the changing scan rates, which suggests surface-controlled or diffusion-

Table 1

Comparison of areal and gravimetric specific capacitances of this work measured in two and three-electrode configurations with various similar materials for flexible supercapacitor application.

Sample	Measurement configuration	Current density	Electrolyte	Areal Capacitance (mF/cm^2)	Ref.
MoS_2@CNT/RGO	Two-electrode	0.1 mA/cm^2	H_2SO_4/PVA	29.5	[26]
MoS_2@CNT/RGO	Single electrode	0.1 mA/cm^2	H_2SO_4/PVA	128	[26]
RGO+CNT@CMC	Single electrode	1 mA/cm^2	H_2SO_4/PVA	177	[53]
MoS_2/CNT	Single electrode	5 mV/s	Na2SO4	337	[28]
MoS_2/CNT	Two-electrode	5 mV/s	Na2SO4	131	[28]
MoS_2/PANI/CNT	Two-electrode	0.5 Na2SO4	H_2SO_4/PVA	168	[18]
PANI/MWCNT/PDMS	Single electrode	5 mV/s	PVA/H 2 SO 4	481	[54]
TiO_2/VACNT	Two-electrode	1.69 mA/cm^2	Na2SO4	16.24	[55]
CNT/graphene/PANI	Two-electrode	0.1 mA/cm^2	PVA/H3PO4	261	[56]
CNT/PANi/PDMS	Single electrode	1 mA/cm^2	PVA/H3PO4	408	[29]
CNT/PANi/PDMS	Two-electrode	0.2 mA/cm^2	PVA/H3PO4	40.6	[29]
CNT/MnO_2	Single electrode	0.1 mA/cm^2	Na2SO4	231	[57]
PANI/GO/CNT	Single electrode	1 mA/cm^2	PVA/H3PO4	510	[58]
CNT/SnS_2	Single electrode	1 mA/cm^2	PVA/LiCl	533	Present work
CNT/SnS_2	Two-electrode	1 mA/cm^2	PVA/LiCl	133	Present work

controlled behaviours. Usually, slope = 1 indicates the capacitive nature of charge storage, while slope = 0.5 accounts for a diffusion-controlled process and a slope between 0.5 and 1 indicates a mixed mechanism of charge storage [47]. The fabricated devices show a linear dependence with the scan rate, with slopes of 0.75, 0.88, 0.82, and 0.66 for CNT, CNT-SnS_2, CNT-GO, and CNT-TRG, respectively (Fig. 6e). Therefore, the higher slope for CNT-SnS_2 and CNT-GO accounts for the cumulative redox and EDLC type charge storage behaviours.

The charge storage and transport mechanisms in the resulting CNT hybrids supercapacitor devices were further investigated via EIS analysis (Fig. 6f). All the CNT hybrid samples behave as ideal capacitors, with no contribution in the high-frequency region [48]. For the pristine CNT and CNT-TRG-based supercapacitor devices, there are small, deviated lines with slopes near to 1 in the middle frequency region, demonstrating more excellent Warburg/diffusion resistances than those of the CNT-SnS_2 and CNT-GO based devices. Similarly, small semicircles are observed in the high-frequency region for CNT-SnS_2, and CNT-GO-based devices, signifying the charge transfer resistances originated by possible redox reactions of SnS_2 and GO, respectively [49]. The intersection of Nyquist plots with the real axis represents an internal resistance of a CNT hybrid symmetric hybrid supercapacitors, correlating to the electrode conductivity and the ionic conductivity of the electrolyte. The internal resistance decreases with the addition of more functional redox-active 2D materials, such as SnS_2 and GO (CNTSnS$_2$ = 7.3 Ω, and CNT–GO = 10.9 Ω). The CNT-SnS_2 hybrid shows lower internal resistance likely due to the interaction of 2D SnS_2 nanosheets with CNTs and their hierarchical alignments (Fig. 2a). Hence, the synergy between CNT and SnS_2 nanosheets leads to the improved conductive network at the electrode interface and to a better ionic interaction from the electrolyte. On the contrary, the higher internal resistance in the CNT-TRG-based devices (CNT-TRG = 13.4 Ω) could be ascribed due to the high degree of TRG agglomeration and its possible pore clogging effect on CNTs, causing hindrance for faster ion diffusion. According to the BET analysis (Fig. 3b), CNT/TRG-based electrodes show lower surface area in regards with the other samples, while morphologically uneven, as shown in Fig. S3 [50]. A modified Randles equivalent circuit for these plots is shown in Fig. S5. The C_{dl} and C_{sf} are possibly the double-layer capacitance (EDLC) and pseudo-capacitance by the surface faradaic process, respectively. Whereas W represent the Warburg resistance and R_s, R_{ct} and R_{sf} denotes the combined series resistance, charge-transfer resistance, and surface resistance, respectively [51].

The symmetric electrode configuration for a supercapacitor is considered an effective approach to achieving the optimal power and energy density with a semi-solid electrolyte type that widens the broad operating voltage window [52]. Therefore, selecting the right composition and load of the electrode materials is imperative for improved performance. In this work, a symmetric all-solid-state and flexible

supercapacitor device were assembled using CNT hybrids films as positive and negative electrodes, and PVA-LiCl gel served as both electrolyte and separator as discussed in Section 2.5 and illustrated in Fig. 7a. To investigate the charge storage performances of the resulting devices, the galvanostatic charge-discharge (GCD) cycles were performed at different current densities. Fig. 7b shows the GCD curves measured at 3 mA/cm^2 for all the CNT hybrid-based supercapacitor devices. All GCD curves of the CNT hybrid flexible symmetric supercapacitor mostly follow the linear and symmetrical pattern with exception of CNT-GO, which slightly shows a pseudocapacitive non-linear type GCD pattern. Overall, GCD reveals that the double-layer capacitance behaviour of the CNTs is dominant with some redox-type contributions from SnS_2 and GO, which is in accordance with CV measurements shown in Fig. 6a-d. The GCD behaviour of all the CNT hybrid devices in response to different current densities is presented in Fig. S6. All the devices follow similar GCD trends as described in Fig. 7b. However, for CNT-TRG, which at low charging current strives to attain the applied voltage due to its disruptive porous structure and low surface area (Fig. 3b). Similarly, the estimated areal and volumetric capacitances for the CNT hybrid electrodes as a function of applied current (Fig. 7c and Fig. S8) shows how the CNT-SnS_2 hybrid electrode has higher charge-storage performance over other electrodes. Specifically, at a current density of 3 mA/cm^2, the CNT-SnS_2 hybrid electrode showed the highest areal capacitance of 533 mF/cm^2 and volumetric capacitance of 63 mF/cm^3. Also, in symmetric device configuration, the CNT/SnS_2-based device showed the highest areal capacitance i.e. 133 mF/cm^2 (Fig. 7d) and vol. the capacitance of 15.7 mF/cm^3 (Fig. S7 and S8). Notably, the obtained results are comparable with or higher than those of the recently reported CNT-based FSSCs (Table-1). Such improved charge storage performance of CNT/SnS_2 was attributed to the highly porous network formed by the addition of 2D SnS_2 nanosheets as well as a contribution from its redox behaviour. However, in terms of the rate capability, CNT-GO performs better delivering the high-rate capability of around 66 % at a remarkably high current 20 mA. Interestingly, the CNT-TRG hybrids electrode showed lower charge storage performance which was further reduced at high current. Such unanticipated behaviour could be attributed due to the possible blocking of CNT pores by poorly dispersed TRG sheets leading to the low surface area, which creates the tortuous path for the ion diffusions, especially at high charging-discharging current. Accordingly, the accessible surface area diminishes CNT-GO>CNT-SnS_2>CNT>CNT-TRG. This behaviour for CNT-TRG was supported by the SEM and BET surface area analysis presented in Fig. S2 and Fig. 3b, respectively.

The capacitance behaviour of our best performing CNT-SnS_2 flexible free-standing single electrode and the assembled symmetric supercapacitor device was compared with other CNT nanohybrid-based flexible supercapacitor devices and summarized in Table 1. It can be seen that the CNT-SnS_2 hybrid electrodes possess high areal capacitance
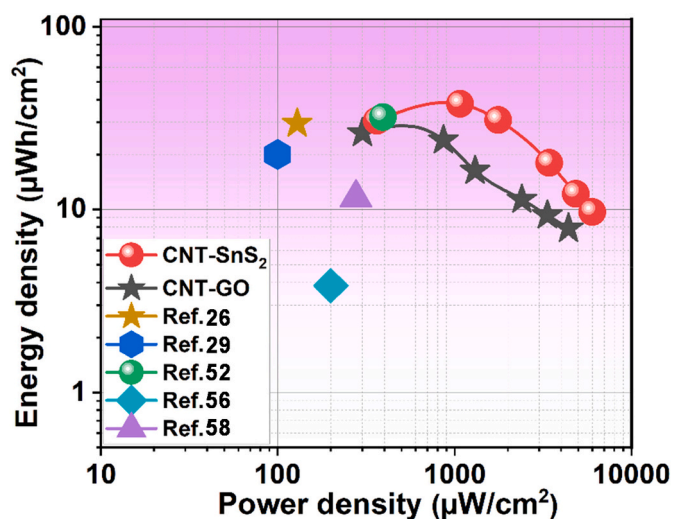
Fig. 8. Ragone plots of areal energy density versus areal power density results for the CNT-SnS$_2$ and CNT-GO FSSS devices in comparison with similar literature reports.

over the other materials.

The Ragone plot, which can validate the capability of the CNT hybrid device for actual power source applications is presented in Fig. 7e. Among the assembled CNT hybrid-based devices, the CNT-SnS$_2$ hybrid exhibits the highest areal energy and areal power density over other CNT hybrids following the sequence of CNT-SnS$_2$, CNT-GO, CNT-TRG, and pristine CNTs. The CNT-SnS$_2$ FSSSC device comparatively reaches a power density of 6000 µWh/cm^2 i.e. 6 mWh/cm^2 at an energy density of 10 µWh/cm^2. Similarly, the device achieves a maximum energy density

of 38 µWh/cm^2 at a power density of 1066 µWh/cm^2. When related to the literature the results obtained from CNT-SnS$_2$ and CNT-GO-based devices are comparable with or even higher than those of the recently reported CNT-based flexible SCs as presented in Fig. 8 [26,29,53,57,59]. The electrochemical performance of these devices is particularly attributed to the tailored porous structure and induced redox properties, which are resultant of targeted purposive design.

As termed flexible supercapacitors, the fabricated CNT hybrid supercapacitors necessitate the assessment of electrochemical performance under bending/folding without compromising their structural integrity. The highest performing CNT-SnS$_2$-based device was chosen for the bending studies (Fig. 9). The device was subjected to the highest bending angle i.e. 180° and properties were compared with the flat device as displayed in Fig. 9a. Similarlry, the Fig. 9b demonstrates the symmetrical rectangular CV patterns of the device before and after bending with no drastic changes indicating the unchanged electrochemical performance upon bending. Similarly, GCD curves presented in Fig. 9c show a typical triangular symmetric shape for both the devices implying excellent capacitive behaviour. The bent sample does show slightly higher discharge time but at the expense of elevated internal resistance. Electrochemical impedance data (Fig. 9d), shows a similar diffusion pattern in the low-frequency region whereas, at high frequency, the bending introduces a, however little, increase in charge transfer resistance, which is inevitable considering the remarkably high bending angle of the device. The long-term cycling stability of the supercapacitor was assessed over a continuous cyclic charge-discharge process at a fixed current density of 2 mA/cm^2, (Fig. 9e). The SnS$_2$ infused supercapacitor device, under 180° bend, retains almost 85 % of the initial areal capacitance after 5000 GCD cycles, with long-term cycling stability. The inset figure reveals the first 5 and last 5 GCD cycles showing no significant electrochemical change during the long-term charging and discharging process after cycling 5000 times. The
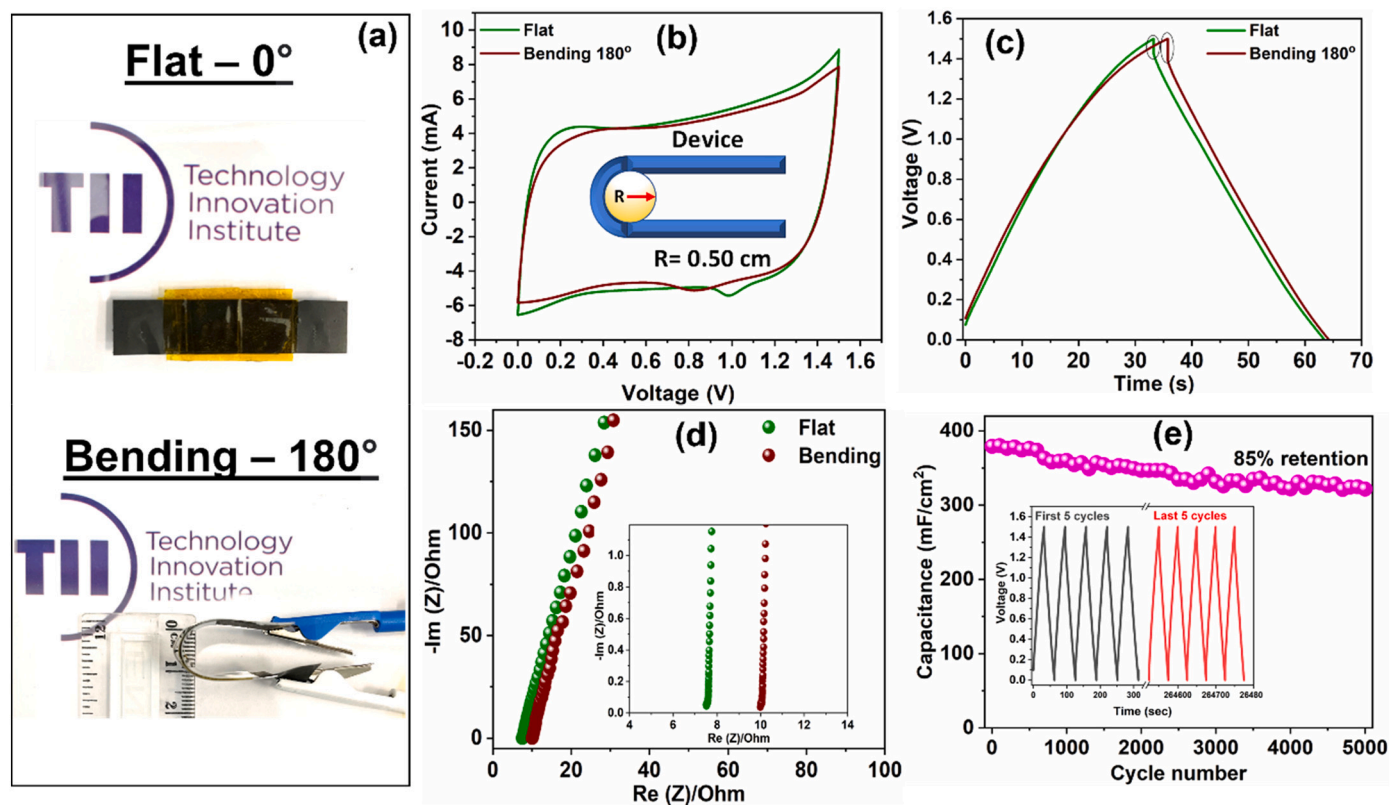
Fig. 9. The pictures of flat and large angle folded flexible supercapacitor based on CNT-SnS$_2$ electrodes (a), CV curves at a scan rate of 50 mV/s (b) the charge-discharge curves at 5 mA. cm^{-2} (c), Nyquist plots (inset is the high-frequency region) (d) before and after bending the device for 180°, and the cycling stability after 5000 cycles (inset is the first five and last five GCD cycles (e).
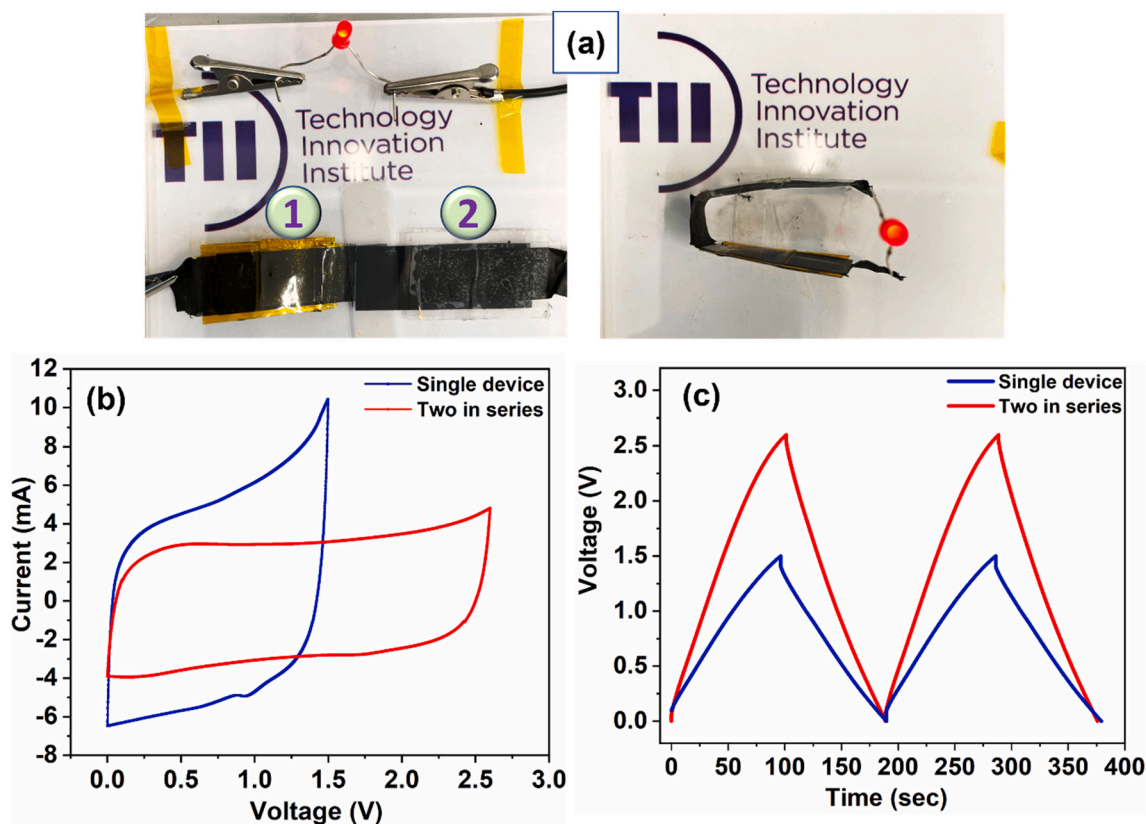
Fig. 10. Two in one connected flexible SSC based in PVA-LiCl gel electrolyte and LED powered by the tandem device (a), CV curves (b), and GCD curves (c) of single and two-in-series devices at the scan rate of $50\,mV\,s^{-1}$ and 2 mA. cm^{-2} current density, respectively.

morphology of the hybrid electrode after the cyclic stability showed a slightly modified structural feature, together with initial pulverisation of the SnS_2 sheets (Fig. S9).

In real-time applications, the portable types of equipment requiring higher voltages use device packs with two or more devices connected in series. Adding electrochemical capacitors together in a serial loop enhances the voltage range, while the current remains the same. Herein, the performance of a CNT-SnS_2 hybrid-based all-solid-state electrochemical capacitor pack with two devices connected in series was tested as displayed in Fig. 10a. The CV curves (Fig. 10b) scanned at 50 mV/s show that the voltage can be extended up to 2.6 V effortlessly, while the produced current (represented by the area under the curve) is the same for the single device and the cell pack. Fig. 10c shows the charge/discharge curves for a single device and the cell pack were all operated under the same constant current conditions. As can be seen at the same charge/discharge current, the voltage is extended from 1.5 V for a single device to 2.6 V for a cell pack. Interestingly, a little voltage drop is observed in the GCD curves of the 2-in-1 series device pack indicating low internal resistance. This helps optimize the useful energy that can be drawn from the device. The as-obtained 2-in-1 series pack efficiently power the red light-emitting diode (LED) under both flat and bending configurations (Fig. 10a), demonstrating the high potential of such supercapacitors in flexible power sources.

4. Conclusions

In this work, we have investigated the effect of the selected 2D materials infusion into commercial CNTs on energy storage applications. The energy-active 2D materials such as SnS_2, GO, and TRG were facilely introduced into the CNT matrix using the scalable ultrasonic dispersion method. Also, a simple tape casting was used to obtain the free-standing flexible CNT nonhybrids films. The resulting hybrid films were used as electrode materials along with PVA/LiCl gel electrolyte cum separator to assemble the flexible all-solid-state-symmetric supercapacitor device. The CNT hybrids electrode exhibited both EDLC and pseudocapacitive charge storage mechanisms. The CNT-SnS_2 hybrid electrodes were observed to hold a high areal capacitance of 533 mF/cm^2, whereas the symmetric device achieved the highest capacitance of 133 mF/cm^2. Moreover, the assembled device shows high cyclic stability with excellent performance under bending. Hence, the facile introduction of 2D materials into industrial-grade CNT nanostructures results in a hybrid structure that yields competitive electrochemical performance with great potential for flexible electronics and portable energy storage applications.

CRediT authorship contribution statement

Sunil P. Lonkar: Conceptualization, Methodology, Experimental, characterization, writing-original draft preparation; **Zainab Karam**-Methodology; Abdulrahman Alshaya-**Experimental; Myriam Ghodh-bane**: Characterization; **Juveiriah M. Ashraf**- Characterization; **Vincenzo Giannini** - Reviewing and Editing; **Chiara Busa** - Reviewing and Editing.

Declaration of competing interest

The authors declare that they have no known competing financial interests or personal relationships that could have appeared to influence the work reported in this paper.

Data availability

Data will be made available on request.

Acknowledgments

Appendix A. Supplementary data

Supplementary data to this article can be found online at https://doi.org/10.1016/j.est.2022.106257.

References

[1] Y. Gu, T. Zhang, H. Chen, F. Wang, Y. Pu, C. Gao, S. Li, Mini review on flexible and wearable electronics for monitoring human health information, Nanoscale Res. Lett. 14 (2019) 263.

[2] D. Baran, D. Corzo, G. Blazquez, Flexible electronics: status, challenges and opportunities, Front.Electron. 1 (2020).

[3] C. Yu, J. An, Q. Chen, J. Zhou, W. Huang, Y.-J. Kim, G. Sun, Recent advances in design of flexible electrodes for miniaturized supercapacitors, Small Methods 4 (2020) 1900824.

[4] K. Keum, J.W. Kim, S.Y. Hong, J.G. Son, S.-S. Lee, J.S. Ha, Flexible/stretchable supercapacitors with novel functionality for wearable electronics, Adv. Mater. 32 (2020), 2002180.

[5] T. An, W. Cheng, Recent progress in stretchable supercapacitors, J. Mater. Chem. A 6 (2018) 15478–15494.

[6] D.P. Dubal, N.R. Chodankar, D.-H. Kim, P. Gomez-Romero, Towards flexible solid-state supercapacitors for smart and wearable electronics, Chem. Soc. Rev. 47 (2018) 2065–2129.

[7] Y.Y. How, A. Numan, M.N. Mustafa, R. Walvekar, M. Khalid, N.M. Mubarak, A review on the binder-free electrode fabrication for electrochemical energy storage devices, J.Energy Storage 51 (2022), 104324.

[8] K. Shen, S. Zhai, S. Wang, Q. Ru, X. Hou, K. San Hui, K. Nam Hui, F. Chen, Recent progress in binder-free electrodes synthesis for electrochemical energy storage application, BatteriesSupercaps 4 (2021) 860–880.

[9] L. Jiang, L. Yuan, W. Wang, Q. Zhang, Soft materials for wearable supercapacitors, Soft Sci. 1 (2021) 5.

[10] L. Liu, Z. Niu, J. Chen, Flexible supercapacitors based on carbon nanotubes, Chin. Chem. Lett. 29 (2018) 571–581.

[11] S. Zhu, J. Ni, Y. Li, Carbon nanotube-based electrodes for flexible supercapacitors, Nano Res. 13 (2020) 1825–1841.

[12] L. Xiang, H. Zhang, Y. Hu, L.-M. Peng, Carbon nanotube-based flexible electronics, J. Mater. Chem. C 6 (2018) 7714–7727.

[13] Y. Luo, K. Wang, Q. Li, S. Fan, J. Wang, Macroscopic carbon nanotube structures for lithium batteries, Small 16 (2020) 1902719.

[14] D.F. Alvarenga, M.G. Junior, M.C.G. Santos, P.S. Pinto, T.H.R. da Cunha, M.C. Dias, R.L. Lavall, P.F.R. Ortega, Tuning carbon nanotube-based buckypaper properties by incorporating different cellulose nanofibrils for redox supercapacitor electrodes, J.Energy Storage 52 (2022), 104848.

[15] T. De Silva, C. Damery, R. Alkhaldi, R. Karunanithy, D.H. Gallaba, P.D. Patil, M. Wasala, P. Sivakumar, A. Migone, S. Talapatra, Carbon nanotube based robust and flexible solid-state supercapacitor, ACS Appl. Mater. Interfaces 13 (2021) 56004–56013.

[16] B. Brown, B. Swain, J. Hiltwine, D.B. Brooks, Z. Zhou, Carbon nanosheet buckypaper: a graphene-carbon nanotube hybrid material for enhanced supercapacitor performance, J. Power Sources 272 (2014) 979–986.

[17] K. Yang, K. Cho, S. Kim, Electrochemical characteristics of flexible micro supercapacitors with reduced graphene oxide-carbon nanotubes composite electrodes, Superlattice. Microst. 118 (2018) 145–151.

[18] I.W.P. Chen, Y.-C. Chou, P.-Y. Wang, Integration of ultrathin MoS2/PANI/CNT composite paper in producing all-solid-state flexible supercapacitors with exceptional volumetric energy density, J. Phys. Chem. C 123 (2019) 17864–17872.

[19] Z. Pan, J. Yang, Q. Zhang, M. Liu, Y. Hu, Z. Kou, N. Liu, X. Yang, X. Ding, H. Chen, J. Li, K. Zhang, Y. Qiu, Q. Li, J. Wang, Y. Zhang, All-solid-state fiber supercapacitors with ultrahigh volumetric energy density and outstanding flexibility, Adv. Energy Mater. 9 (2019) 1802753.

[20] O. Moradlou, H. Sharifpour, Interconnected NiCo2S4 - coated NiO nanosheet arrays as electrode materials for high-performance supercapacitors, J.Energy Storage 32 (2020), 101886.

[21] K.T. Kubra, R. Hafeez, G. Ali, H. Ahmad, A. Butt, A. Salman, R. Sharif, M. Sultana, M. Bashir, Electrochemical investigation of a novel quaternary composite based on dichalcogenides, reduced graphene oxide, and polyaniline as a high-performance electrode for hybrid supercapacitor applications, J. Alloys Compd. 909 (2022), 164854.

[22] M.S. Javed, H. Lei, Z. Wang, B.-T. Liu, X. Cai, W. Mai, 2D V2O5 nanosheets as a binder-free high-energy cathode for ultrafast aqueous and flexible Zn-ion batteries, Nano Energy 70 (2020), 104573.

[23] M.S. Javed, S.S.A. Shah, S. Hussain, S. Tan, W. Mai, Mesoporous manganese-selenide microflowers with enhanced electrochemical performance as a flexible symmetric 1.8 V supercapacitor, Chem. Eng. J. 382 (2020), 122814.

[24] M.S. Javed, S.S.A. Shah, T. Najam, S.H. Siyal, S. Hussain, M. Saleem, Z. Zhao, W. Mai, Achieving high-energy density and superior cyclic stability in flexible and

[25] M.S. Javed, N. Shaheen, S. Hussain, J. Li, S.S.A. Shah, Y. Abbas, M.A. Ahmad, R. Raza, W. Mai, An ultra-high energy density flexible asymmetric supercapacitor based on hierarchical fabric decorated with 2D bimetallic oxide nanosheets and MOF-derived porous carbon polyhedra, J. Mater. Chem. A 7 (2019) 946–957.

[26] S. Wang, J. Zhu, Y. Shao, W. Li, Y. Wu, L. Zhang, X. Hao, Three-dimensional MoS2@CNT/RGO network composites for high-performance flexible supercapacitors, <sb:contribution><sb:title>Chem.</sb:title></sb:contribution><sb:host><sb:issue><sb:series><sb:title>Eur. J.</sb:title></sb:series></sb:issue></sb:host> 23 (2017) 3438–3446.

[27] W. Zhou, J. Miao, X. Yan, Y. Li, Y. Zhu, W. Zhang, M. Zhang, W. Zhu, M.S. Javed, J. Pan, S. Hussain, SnS2 nanosheet arrays anchoring on functionalized carbon cloth for quasi-solid-state flexible supercapacitor with satisfactory electrochemical performance and mechanical stability, Nanotechnology 32 (2021), 505408.

[28] P. Tiwari, J. Jaiswal, R. Chandra, Hierarchal growth of MoS2@CNT heterostructure for all solid state symmetric supercapacitor: insights into the surface science and storage mechanism, Electrochim. Acta 324 (2019) 134767.

[29] R.D.C. Balboni, G.K. Maron, M.G. Masteghin, M.O. Tas, L.S. Rodrigues, V. Gehrke, J.H. Alano, R. Andreazza, N.L.V. Carreño, S.R.P. Silva, An easy to assemble PDMS/CNTs/PANI flexible supercapacitor with high energy-to-power density, Nanoscale 14 (2022) 2266–2276.

[30] X. Yang, J. Li, C. Hou, Q. Zhang, Y. Li, H. Wang, Skeleton-structure WS2@CNT thin-film hybrid electrodes for high-performance quasi-solid-state flexible supercapacitors, Front.Chem. 8 (2020).

[31] D. Wang, X. Yan, C. Zhou, J. Wang, X. Yuan, H. Jiang, Y. Zhu, X. Cheng, R. Li, A free-standing electrode based on 2D SnS2 nanoplates@3D carbon foam for high performance supercapacitors, Int. J. Energy Res. 44 (2020) 8542–8554.

[32] M. Ojha, S. Naskar, B. Kaur, A. Kolay, M. Deepa, Lithiated tin di-sulfide micro-flowers with expanded interlayer spaces coupled with bakelite-carbon for an enhanced performance supercapacitor, J.Energy Storage 44 (2021), 103463.

[33] M. Setayeshmehr, M. Haghighi, K. Mirabbaszadeh, A review of tin disulfide (SnS2) composite electrode materials for supercapacitors, Energy Storage 4 (2022), e295.

[34] S.P. Lonkar, V.V. Pillai, S.P. Patole, S.M. Alhassan, Scalable in situ synthesis of 2D-3D graphene-wrapped SnS2 nanohybrids for enhanced supercapacitor and electrocatalytic applications, ACS Appl.Energy Mater. 3 (2020) 4995–5005.

[35] S.P. Lonkar, V.V. Pillai, S. Stephen, A. Abdala, V. Mittal, Facile in situ fabrication of nanostructured graphene–CuO hybrid with hydrogen sulfide removal capacity, Nano-Micro Lett. 8 (2016) 312–319.

[36] Y.-J. Gu, W. Wen, J.-M. Wu, Simple air calcination affords commercial carbon cloth with high areal specific capacitance for symmetrical supercapacitors, J. Mater. Chem. A 6 (2018) 21078–21086.

[37] S. Wang, R.A.W. Dryfe, Graphene oxide-assisted deposition of carbon nanotubes on carbon cloth as advanced binder-free electrodes for flexible supercapacitors, J. Mater. Chem. A 1 (2013) 5279–5283.

[38] A. Cao, C. Xu, J. Liang, D. Wu, B. Wei, X-ray diffraction characterization on the alignment degree of carbon nanotubes, Chem. Phys. Lett. 344 (2001) 13–17.

[39] J.A. Rojas, L.A. Ardila-Rodríguez, M.F. Diniz, M. Gonçalves, B. Ribeiro, M.C. Rezende, Highly porous multiwalled carbon nanotube buckypaper using electrospun polyacrylonitrile nanofiber as a sacrificial material, Heliyon 5 (2019), e01386.

[40] D.B. Schuepfer, F. Badaczewski, J.M. Guerra-Castro, D.M. Hofmann, C. Heiliger, B. Smarsly, P.J. Klar, Assessing the structural properties of graphitic and non-graphitic carbons by Raman spectroscopy, Carbon 161 (2020) 359–372.

[41] S. Azizighannad, S. Mitra, Controlled synthesis of reduced graphene oxide-carbon nanotube hybrids and their aqueous behavior, J. Nanopart. Res. 22 (2020) 130.

[42] Y. Jiang, D. Song, J. Wu, Z. Wang, S. Huang, Y. Xu, Z. Chen, B. Zhao, J. Zhang, Sandwich-like SnS2/graphene/SnS2 with expanded interlayer distance as high-rate lithium/sodium-ion battery anode materials, ACS Nano 13 (2019) 9100–9111.

[43] W.G. Nunes, B.G.A. Freitas, R.M. Beraldo, R.M. Filho, L.M. Da Silva, H. Zanin, A rational experimental approach to identify correctly the working voltage window of aqueous-based supercapacitors, Sci. Rep. 10 (2020) 19195.

[44] M. Setayeshmehr M. Haghighi K. Mirabbaszadeh A review of tin disulfide (SnS2) composite electrode materials for supercapacitors, Energy Storage, n/a.

[45] B. Xu, S. Yue, Z. Sui, X. Zhang, S. Hou, G. Cao, Y. Yang, What is the choice for supercapacitors: graphene or graphene oxide? Energy Environ. Sci. 4 (2011) 2826–2830.

[46] Q. Li, S. Sun, A.D. Smith, P. Lundgren, Y. Fu, P. Su, T. Xu, L. Ye, L. Sun, J. Liu, P. Enoksson, Compact and low loss electrochemical capacitors using a graphite/carbon nanotube hybrid material for miniaturized systems, J. Power Sources 412 (2019) 374–383.

[47] X. Pu, D. Zhao, C. Fu, Z. Chen, S. Cao, C. Wang, Y. Cao, Understanding and calibration of charge storage mechanism in cyclic voltammetry curves, Angew. Chem. Int. Ed. 60 (2021) 21310–21318.

[48] B.-A. Mei, O. Munteshari, J. Lau, B. Dunn, L. Pilon, Physical interpretations of Nyquist plots for EDLC electrodes and devices, J. Phys. Chem. C 122 (2018) 194–206.

[49] T.S. Mathis, N. Kurra, X. Wang, D. Pinto, P. Simon, Y. Gogotsi, Energy storage data reporting in perspective—guidelines for interpreting the performance of electrochemical energy storage systems, Adv. Energy Mater. 9 (2019), 1902007.

[50] N.O. Laschuk, E.B. Easton, O.V. Zenkina, Reducing the resistance for the use of electrochemical impedance spectroscopy analysis in materials chemistry, RSC Adv. 11 (2021) 27925–27936.

[51] M.R. Hasyim, R. Rajagopalan, Prediction of discharge performances of pseudocapacitors using their impedance characteristics, J. Electrochem. Soc. 167 (2020), 013536.

[52] M. Ciszewski, A. Koszorek, T. Radko, P. Szatkowski, D. Janas, Review of the selected carbon-based materials for symmetric supercapacitor application, J. Electron. Mater. 48 (2019) 717–744.

[53] L. Kou, T. Huang, B. Zheng, Y. Han, X. Zhao, K. Gopalsamy, H. Sun, C. Gao, Coaxial wet-spun yarn supercapacitors for high-energy density and safe wearable electronics, Nat. Commun. 5 (2014) 3754.

[54] M. Yu, Y. Zhang, Y. Zeng, M.-S. Balogun, K. Mai, Z. Zhang, X. Lu, Y. Tong, Water surface assisted synthesis of large-scale carbon nanotube film for high-performance and stretchable supercapacitors, Adv. Mater. 26 (2014) 4724–4729.

[55] P. Avasthi, A. Kumar, V. Balakrishnan, Aligned CNT forests on stainless steel mesh for flexible supercapacitor electrode with high capacitance and power density, ACS Appl.Nano Mater. 2 (2019) 1484–1495.

[56] X. Liang, L. Zhao, Q. Wang, Y. Ma, D. Zhang, A dynamic stretchable and self-healable supercapacitor with a CNT/graphene/PANI composite film, Nanoscale 10 (2018) 22329–22334.

[57] W. Gong, B. Fugetsu, Z. Wang, I. Sakata, L. Su, X. Zhang, H. Ogata, M. Li, C. Wang, J. Li, J. Ortiz-Medina, M. Terrones, M. Endo, Carbon nanotubes and manganese oxide hybrid nanostructures as high performance fiber supercapacitors, Commun. Chem. 1 (2018) 16.

[58] Q. Jiang, Y. Shang, Y. Sun, Y. Yang, S. Hou, Y. Zhang, J. Xu, A. Cao, Flexible and multi-form solid-state supercapacitors based on polyaniline/graphene oxide/CNT composite films and fibers, Diam. Relat. Mater. 92 (2019) 198–207.

[59] J.P. Jyothibasu, R.-H. Lee, Facile,scalable, eco-friendly fabrication of high-performance flexible all-solid-state supercapacitors, Polymers 10 (2018) 1247.